Electronic Supplementary Information

In-situ observation of the electrochemical lithiation of a single MnO@C nanorod electrode with core/shell structure

Yuqing Qiao[1,2*+], Peng Jia[1,2+], Weiyang Ren[1+], shuaijun Ding[2], Yixuan Wen[1], Xiaoyu Zhang[1], Meirong Xia[1], Changzeng Fan[2], Weimin Gao[1*], Liqiang Zhang[2], Faming Gao[1], Jianyu Huang[2*] and Tongde Shen[2*]

[1]Hebei Key Laboratory of Applied Chemistry, College of Environmental and Chemical Engineering, Yanshan University, 066004 Qinhuangdao, China.

[2]Clean Nano Energy Center, State Key Laboratory of Metastable Materials Science and Technology, Yanshan University, 066004 Qinhuangdao, China.

[+]These authors contributed equally.

*To whom correspondence should be addressed. E-mail: qiaoyq@ysu.edu.cn; weimin.gao@outlook.com; jhuang8@ysu.edu.cn; tdshen@ysu.edu.cn.

Experimental

Materials synthesis

MnO_2 nanorods (NRs) were fabricated through a conventional hydrothermal method.[1, 2] The process includes dissolving 10 mmol of $(NH_2)S_2O_8$ and 10 mmol of $MnSO_4$ in 60 mL deionized water in a beaker to form a solution under magnetic stirring at room temperature (25 °C), adding 0.5 ml H_2SO_4 (0.5 mol L^{-1}) in the solution and agitating the mixture with magnetic stirring for 30 min, treating the mixture in a 100 mL Teflon-lined stainless steel autoclave at 140 °C for 10 h, and filtering and drying the mixture at 80 °C for 6 h under a vacuum. The synthesized MnO_2 NRs were then used as precursor to produce MnO@C NRs by the steps as follow: Dissolving 0.16 g of the MnO_2 NRs in 100 mL 2-amino-2-hydroxymethylpropane-1,3-dio (Tris) solution in a beaker to form mixture at room temperature (25 °C); Adding 0.08 g Pluronic F127 ($EO_{106}PO_{70}EO_{106}$) and 0.08 g dopamine in the mixture with magnetic stirring and agitating for 24 h at room temperature; Filtering and drying the mixture for 6 h at 80 °C under a vacuum; Heating the mixture at 700 °C for 2 h in a pipe-type oven in a nitrogen flow of 10 mL min^{-1}.

Materials characterization

X-ray diffraction pattern was analyzed by a Rigaku D/max 2500pc X-ray diffractometer with Cu-Kα radiation (λ = 0.15418 nm). The specific surface area and pore volume of the sample were determined by nitrogen adsorption-desorption isotherms at 77 K with ASAP-2020e system.

Electrochemical measurements with conventional lithium-ion batteries (LIB)

Electrochemical measurements were conducted in a 2032-type coin cell composed of a working electrode, a lithium foil electrode and a Celgard 2400 (polypropylene mono-film) separator. A commercial electrolyte solution (1 mol L^{-1} $LiPF_6$: ethylene carbonate (EC): diethyl carbonate (DEC) = 1: 1: 1) was employed. The dried MnO@C NRs were mixed with acetylene black and polyvinylidene fluoride (PVDF) at a mass ratio of 8:1:1 and grinded in N-methylpyrrolidonepyrrolidinone (NMP) for

20 min in a mortar to form a slurry. The slurry was coated on a copper foil and dried under an infrared lamp for 1h. The anode sheet was punched to a disk with a diameter of 11 mm. and dried at 120 °C for 12 h under a vacuum. The coating has a thickness of about 20 μm and a mass loading of about 1.0 mg cm^{-2}. Electrochemical performances were performed on a LAND CT3001A multichannel battery testing system.

In-situ nanoscale LIB setup

In this study, the voltage was precisely controlled by a potentiostat (PiciFemto V3ST, produced by Anhui Zeyou Technology Co., Ltd.). As a voltage is applied, the current passing through the sample can be characterized at the same time. The variation of measured current is within about ± 0.3 pA. The voltage applied to the sample is the output voltage of the controller, that is, the programming voltage, and the error bar of the voltage is within ± 4.5 mV. The nanoscale LIB has a two-probe configuration, as shown in Fig.3a.[3-6] The MnO@C NR glued to the aluminum tip was used as the working electrode. The bulk lithium metal coated on the tungsten tip was served as the counter electrode. The naturally formed Li$_2$O layer on the surface of the lithium metal was used as the solid electrolyte. Those electrodes were embedded into a TEM-STM (Transmission Electron Microscopy - Scanning Tunneling Microscopy) holder (Pico Femto FE-F2) inside a glovebox. The assembly was then transferred to an aberration-corrected ETEM (FEI, Titan G2, 300 kV). Before the electrochemical charge/discharge experiments, the working electrode was manipulated to contact with the Li$_2$O electrolyte. With the setup, the lithiation process can be visualized in real-time, when an appropriate operating potential is applied to this nanoscale LIB. Accordingly, the lithiation-induced structural and morphological changes can be tracked in-situ.

This paper presents a MnO@C NR with core/shell structure (CSS) and internal void space (IVS), where MnO NR cores are dispersed inside a hollow carbon layer. A nanoscale LIB was constructed with a single MnO@C NR and the lithiation process and lithiation-induced volume expansion (LIVE) during the electrochemical reaction

were in-situ visualized *via* aberration-corrected environmental transmission electron microscopy (ETEM).

Description of the Supplementary Movies

Description of Movie S1

An in-situ ETEM movie showing the morphology evolution of a MnO@C nanorod (NR) during discharge process (corresponding to **Fig. 3**). The movie was recorded at 1 frame/ second in the TEM bright field (BF) mode, and is played at 118× speed.
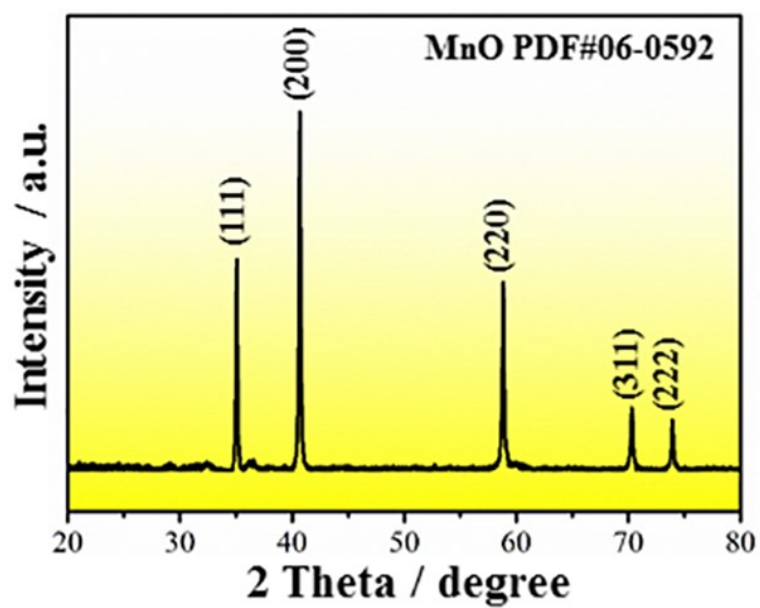
Description of Movie S2

An in-situ ETEM movie showing the morphology evolution of a MnO@C NR during discharge process (corresponding to **Fig. S8**). The movie was recorded at 1 frame/ second in the TEM-BF mode, and is played at 13× speed.

Supplemental Figures

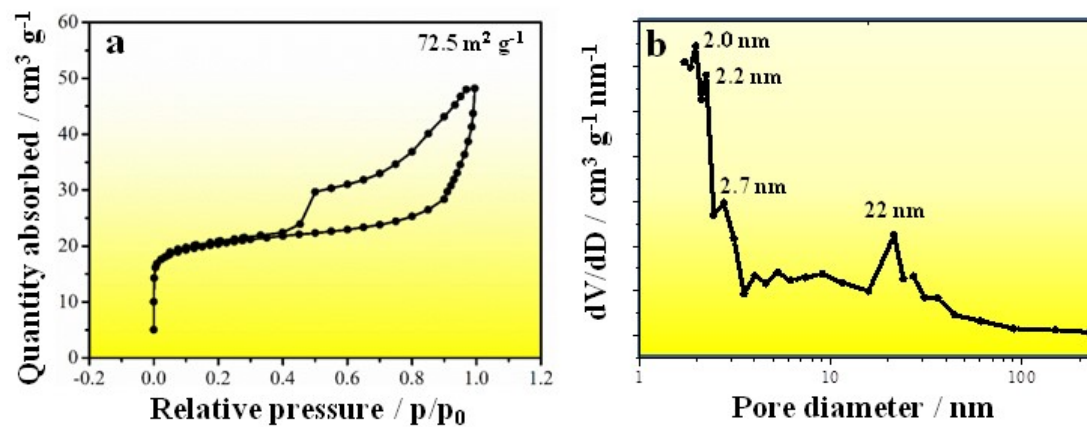**Fig. S1** XRD of the pristine MnO@C NR.

Fig. S2 Nitrogen adsorption/desorption isotherms of the MnO@C electrode materials (a) and the corresponding pore-diameter distribution (b).
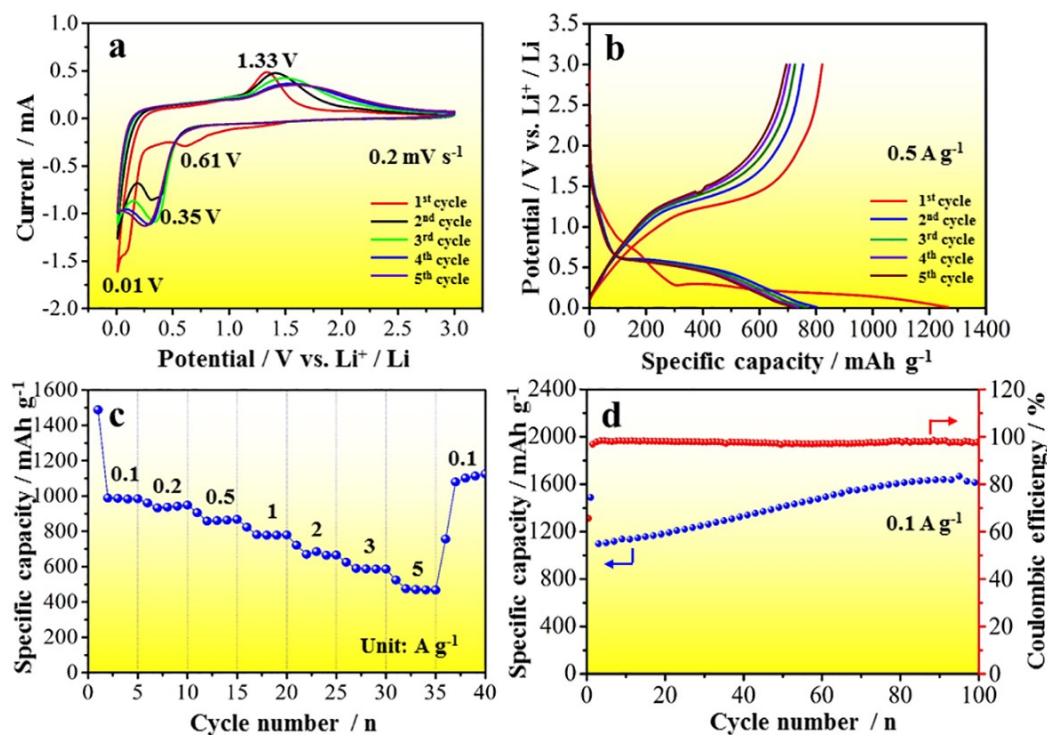
Fig. S3 General electrochemical performance of MnO@C NR used as anode material for Li-ion battery. (a) Cyclic voltammetry curves for the first five cycles at a scan rate of 0.2 mV s^{-1}. (b) Discharge - charge profiles for the first five cycles at a current density of 0.5 A g^{-1}. (c) Rate-capabilities at current density of 0.1-5 A g^{-1}. (d) Performance of 100 cycles and the corresponding coulombic efficiency of the MnO@C electrode material.

The first five cycles of cyclic voltammetry curves of MnO@C NR electrode at 0.2 mV s^{-1} scan rate are displayed in Fig. S3a. The sharp peak of the cathodic scan was at 0.01 V in the first cycle (the red line in a), which was ascribed to the reduction of Mn^{2+} to Mn^0 (MnO + 2Li$^+$ + 2e → Li$_2$O + Mn).[7] It then shifted to 0.35 V in the following cycles, indicating an improved reaction kinetics.[8-11] The small peak at 0.61 V was ascribed to the irreversible reduction of electrolyte, while the anodic peak at 1.33 V was related to the reversible oxidation of Mn^0 to Mn^{2+} (Li$_2$O + Mn → MnO + 2Li$^+$ + 2e) in the initial cycles. No other anodic peak was found, indicating a high reversible capacity of the MnO@C NR electrode. The initial five charge/discharge curves of the MnO@C NR electrode at a current density of 0.5 A g^{-1} were displayed in (Fig. S3b). The well-overlapped curves from the 2nd cycle revealed the structural

integrity for a high cycle stability.[12-14] The MnO@C exhibited a high reversible discharge capacity of 471 mAh g^{-1} at a high current density of 5 A g^{-1}, indicating a high-rate discharge ability (Fig. S3c). In addition, the MnO@C exhibited a higher discharge capacity of 1609 mAh g^{-1} after 100 cycles at a current density of 0.1 A g^{-1}, indicating a high cycle stability. The MnO@C, however, exhibited a low initial coulombic efficiency of 65 % with a discharge capacity of 1532 mAh g^{-1} (Fig. S3d).
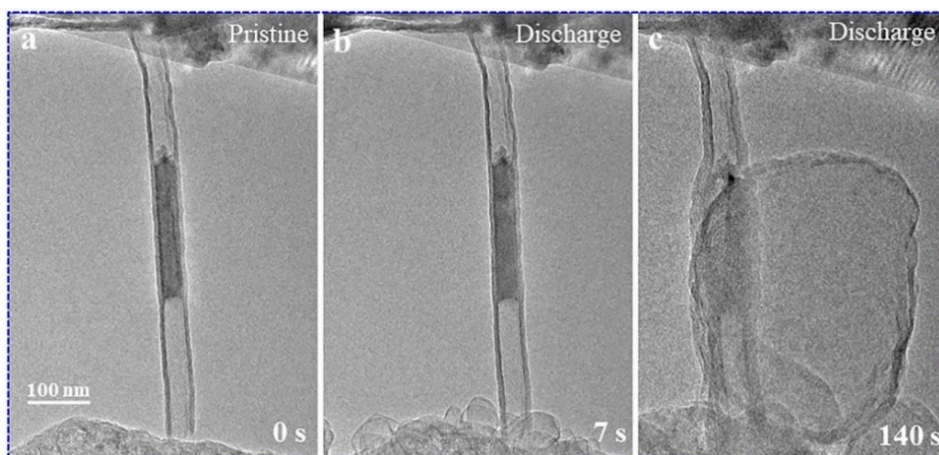
Fig. S4 Structure evolutions of the MnO@C cathode during discharge processes (-3.0 V) in a Li-ion nanobattery.
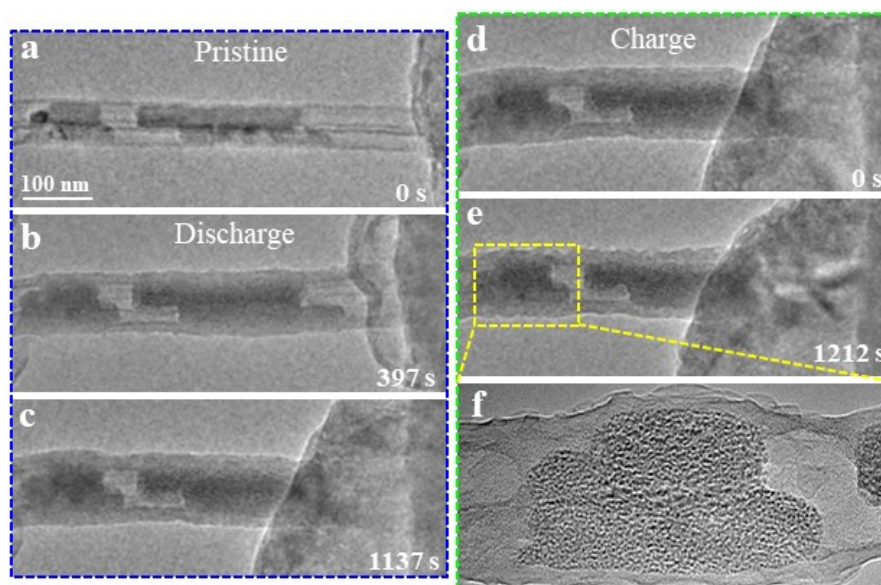

Fig. S5 Structure evolutions of the MnO@C cathode after discharge and charge processes of a Li-ion nanobattery. During the in-situ discharge reaction process, once the structure of the active material is powdered or destroyed, the charging reaction is difficult to restore the active material to its original state.[15, 16]
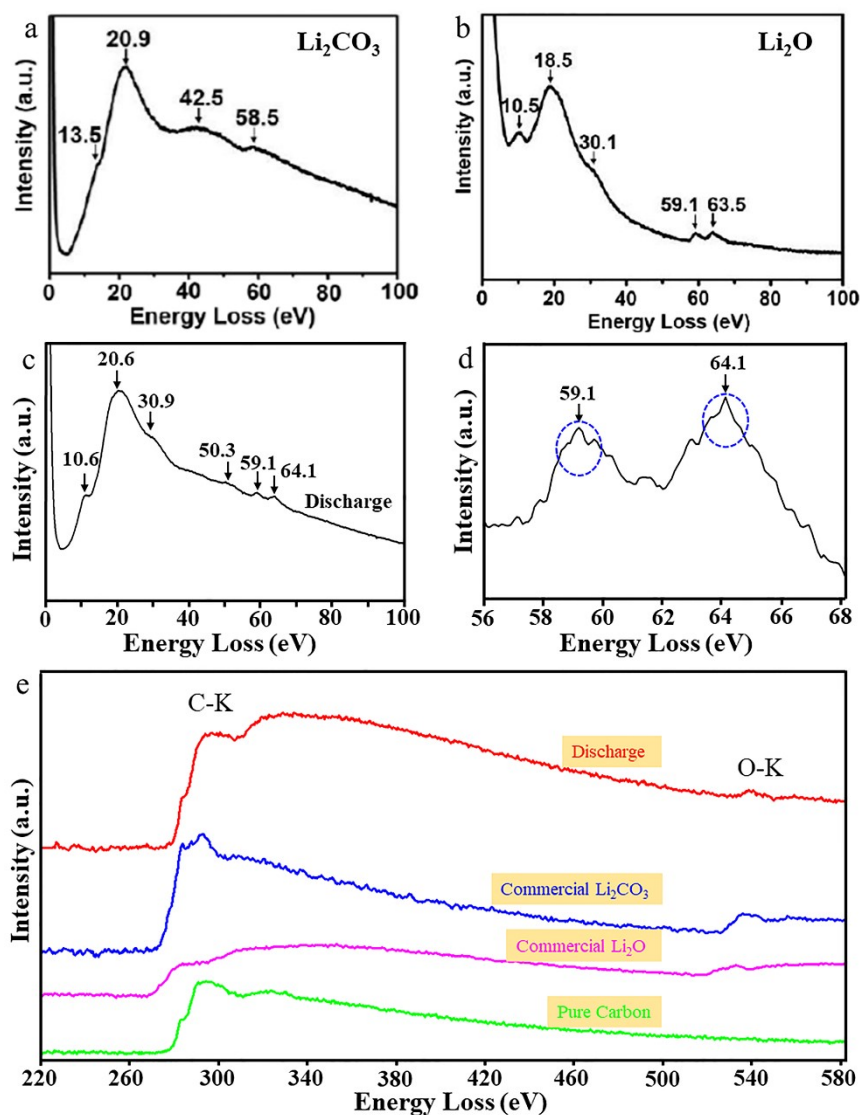
Fig. S6 (a) Low-loss EELS confirm the deposited materials being Li_2CO_3.[17] (b) Low-loss EELS confirm the deposited materials being Li_2O. [17] (c, d) Low-loss EELS of Li_2O in our experiment. (e) Core-loss EELS of discharge products, commercial Li_2CO_3, commercial Li_2O, and pure carbon.

In our discharge experiment, we used low-loss EELS to characterize the discharge products. As shown in Fig. S6c, the main discharge product is Li_2O, and the characteristic peaks of Li_2O are 59.1 and 64.1 eV are observed (Fig. S6d). The peak position of 20.9 eV in Fig. S6a is basically the same as the peak position of 20.6 eV in Fig. S6c,[17] but it does not mean that our discharge product is Li_2CO_3. By using core-loss EELS to analyze our main discharge product Li_2O and commercial Li_2CO_3, we found that the carbon peaks of the two substances are very different, so our discharge

product does not have Li_2CO_3 (Fig. S6e, red and blue lines). The carbon peak of the core-loss EELS of the discharge product is the same as that of pure carbon, because the core-loss EELS signal contains a carbon layer (Fig. S6e, red and green lines). Fig. S6d is basically consistent with the characteristic peaks of Li_2O in Fig. 1d and found in the literature.[18]
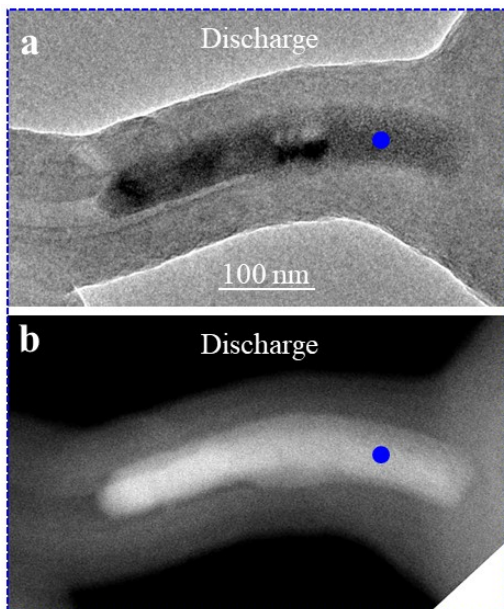

Fig. S7 Time lapse TEM and ADF images of the MnO@C cathode after discharge processes of a Li-ion nanobattery.
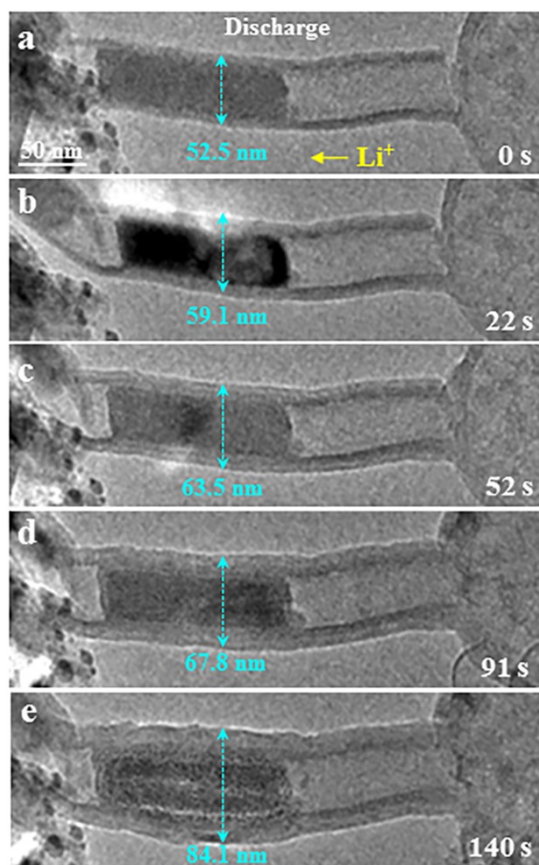
Fig. S8 Structure evolution revealed by in-situ images from another MnO electrode during discharge electrochemical reaction. (a) The initially MnO@C NR. (b-e) Time-lapse volume expansion of the MnO@C.
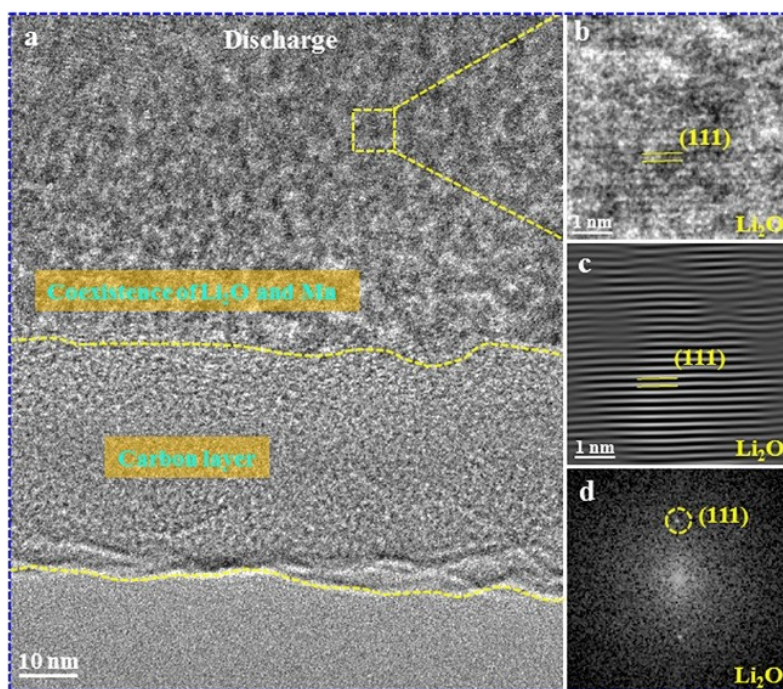
Fig. S9 Microstructure of Mn@Li$_2$O electrode materials after discharge in nanoscale LIBs. (a) HRTEM image showing pulverization coexistence of Li$_2$O and Mn and compactly contact between the amorphous carbon layer and the pulverization Mn@Li$_2$O electrode materials. (b-d) Slightly signals of Li$_2$O in the discharge product: the amplified TEM image, corresponding filter image and FFT image.

Serious pulverization occurred for the MnO electrode materials without the protection of coating carbon layer. The pulverization will lead to the decline of the battery life. The phase interface between the carbon layer and the active electrode materials was also characterized and a compactness contact of the two phases was observed. (Fig. S9a) also indicates an active electrode material with a sponge-like morphology after the initial discharge. Li$_2$O was detected in the product (yellow-box in (Fig. S9a) and the existence was confirmed by the amplified TEM image (Fig. S9b), the corresponding filter image (Fig. S9c) and FFT image (Fig. S9d).
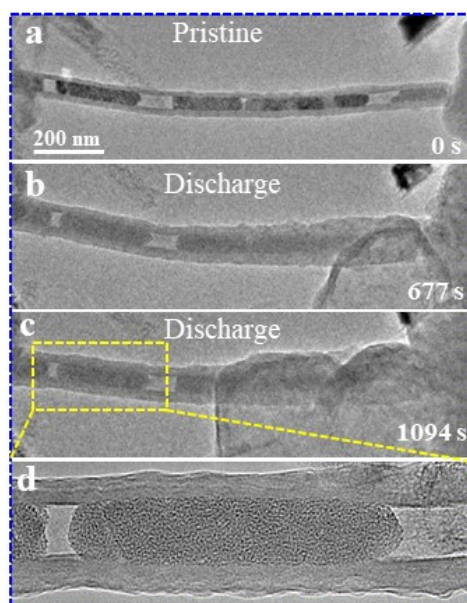
Fig. S10 Time lapse TEM images of the MnO@C cathode after discharge processes of a Li-ion nanobattery.
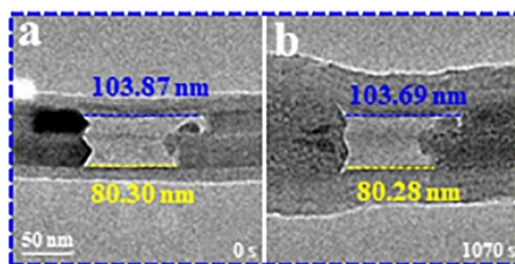

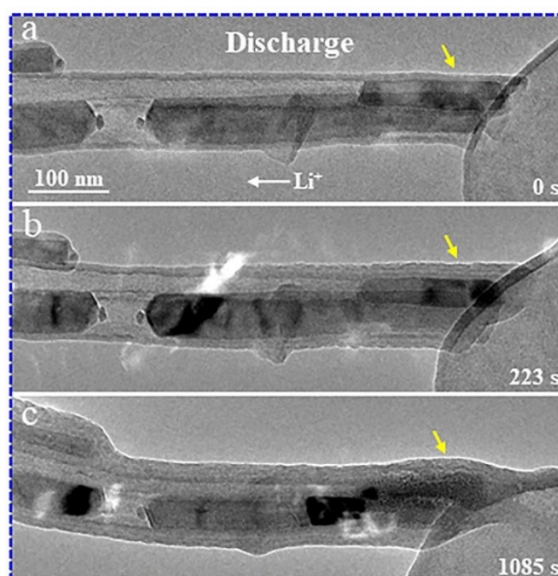**Fig. S11** Time lapse TEM images of the MnO@C cathode after discharge processes of a Li-ion nanobattery.

Fig. S12 Time lapse structure evolution of the MnO@C cathode in a Li-ion nanobattery during discharge processes (-0.5 V).
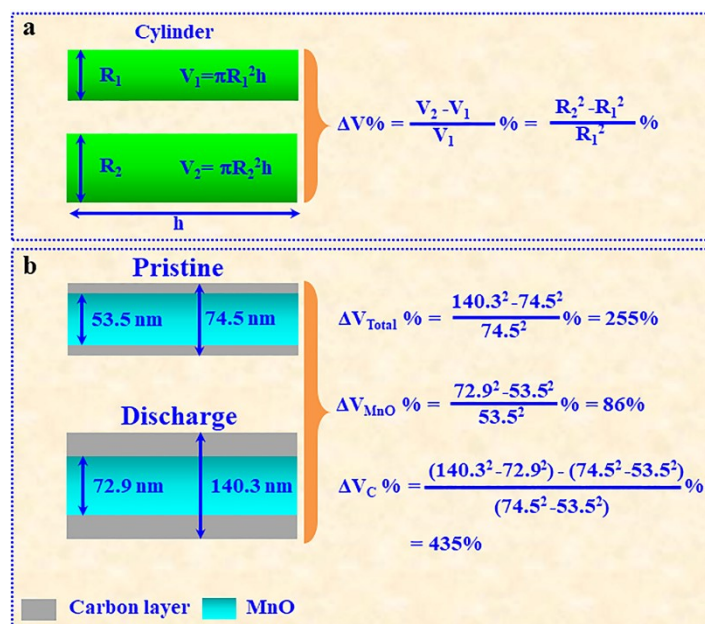
Fig. S13 The relationship between the thickness of the carbon shell and the volume expansion percentage of MnO core.

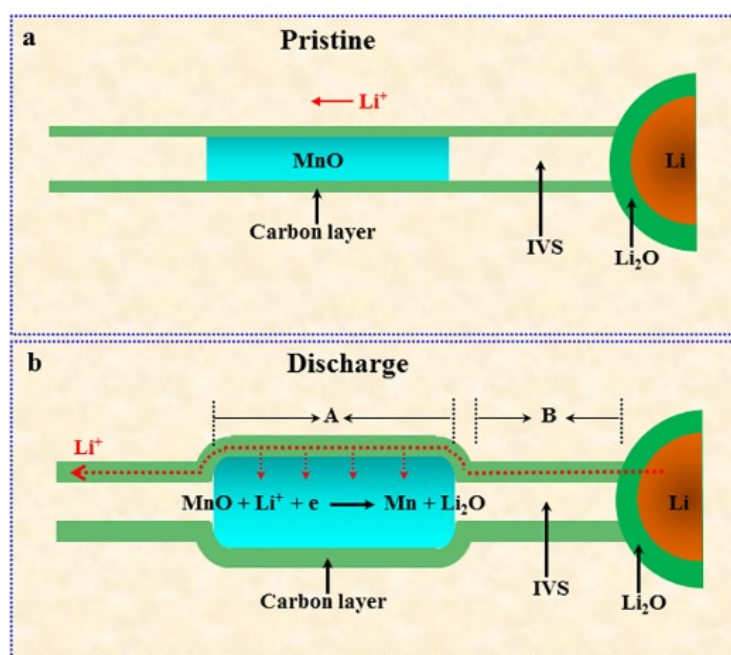**Fig. S14** Schematic of the expansion behavior of a single MnO@C NR electrode during discharge at -0.5 V against a lithium metal electrode, indicating nearly no volume expansion or contraction occurred for the IVS; A-area: a total LIVE of 255 % (435 % for carbon layer and 86 % for MnO); B-area: a total LIVE of 163 % (337 % for carbon layer).

We noted that the time-lapse diameter expansion is non-homogeneous (Fig. 4f).

Although the carbon layer has a uniformly thickness, the diameter expansion of the segment of the carbon layer contacted with IVS (region B in Fig. S14b) was smaller than that of the segment of the carbon layer contacted with MnO (region A in Fig. S14b). the initially diameter increased to 120.9 nm with a smaller total volume expansion of 163 %, and those carbon layer has a smaller volume expansion of about 337 % with a uniform internal diameter (53.5 nm) and a widening external diameter (74.5 nm to 120.9 nm) (Fig. 3b-d). It was reported that the main role of IVS is to accommodate the volume expansion of Transition metal oxide (TMO) active electrode materials during cycling, whereas nearly no volume contraction of the IVS in our experiments was observed.[19-22] The smaller diameter expansion or volume expansion would endow the carbon layer a buffer to relieve the stress of carbon layer, rather than the volume expansion of MnO.
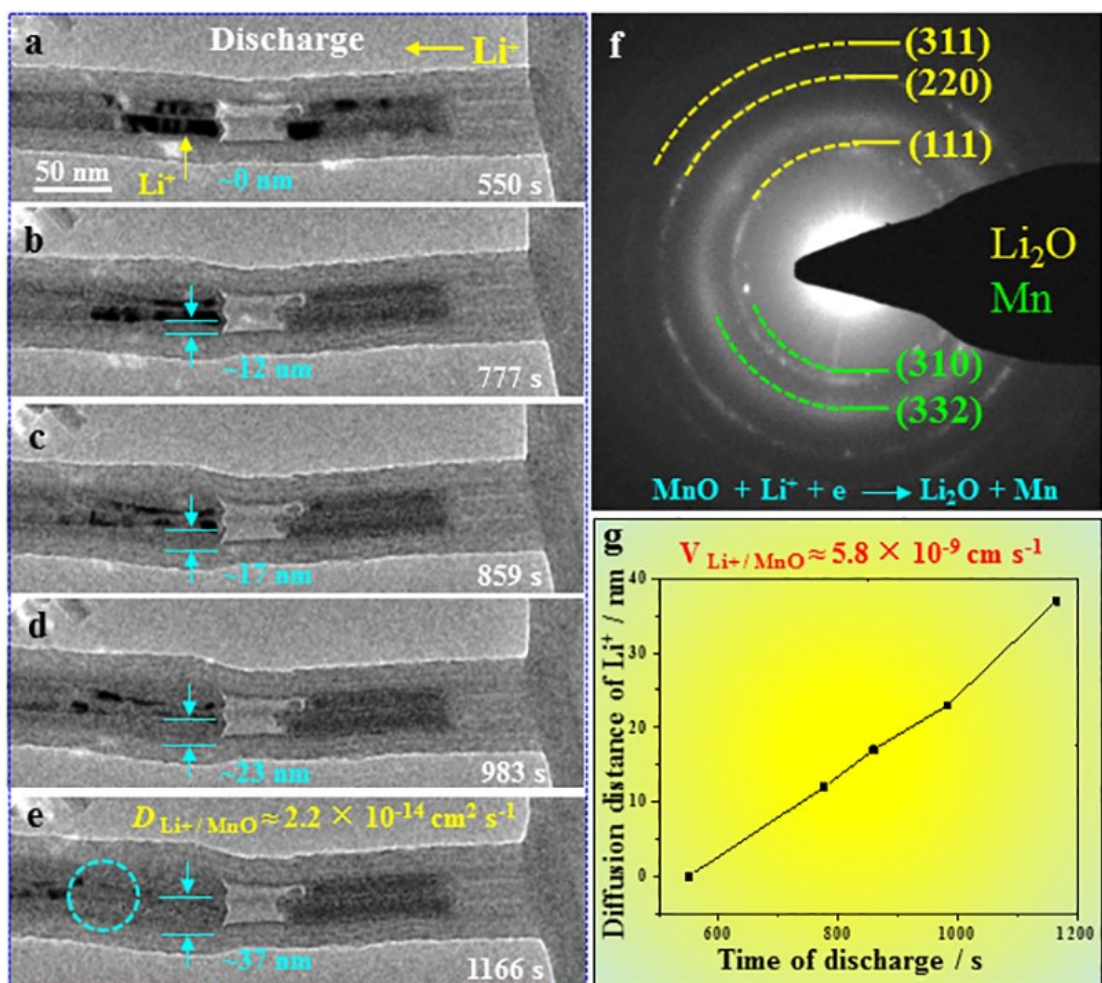
Fig. S15 Structure evolution revealed by in-situ images from a MnO electrode during discharge electrochemical reaction. (a-e) Time-lapse Li-ion diffusion in MnO. (f) EDPs for the discharge product at 1166 s, acquired from the blue-circled region in (e). (g) Relationship between the Li-ion diffusion distance and time of discharge.

In order to investigate the effect of Li^+ insertion on the structural evolution of the MnO@C electrode, time-lapse Li^+ diffuse distance in MnO along the radial direction (Fig. S14, the blue arrow heads in Fig. S15) was examined using the in-situ images taken during discharge (moved 37 nm in 550 s-1166 s, Fig. S15a-e). In this case, it took about 19 min to discharge the MnO@C NR, as confirmed by the weak EDP signals of MnO (Fig. S15f) acquired from the blue-circled region in Fig. S15e. A nearly linear relationship between the expansion distance and discharge time was observed. The Li^+ expansion speed in the MnO core is 5.8×10^{-9} cm s^{-1} (Fig. S15g), which is much smaller than that in the carbon layer.

As we know, porous carbon layer is generally used as a coating material to

improve the electronic conductivity and to relieve the volume expansion of the TMOs electrode materials in electrochemical reaction.[23, 24] To directly visualize its effect on TMOs, a nanoscale processing technique has been used in the present work to construct a nanoscale LIB with a single MnO@C NR. Based on our in-situ observation, the functions of the carbon layer were clarified. The thickness of the carbon layer in our experiment increased from 10.5 to 28.6 nm with a LIVE of 249 % during the electrochemical reaction. This pre-LIVE of carbon layer has never been reported before. Obviously, the pre-LIVE characteristics will increase the tensile strength of the carbon layer to relieve the LIVE of TMOs subsequently and, as a result lead to the long cycle stability. Nearly no volume contraction of the IVS in our experiment was observed, however the carbon layer contacted with IVS revealed a smaller LIVE (337 %) than the carbon layer contacted with TMOs (435 %), that is, the IVS in our experiment was responsible for relieving the stress of carbon layer caused by the LIVE of MnO, rather than providing free spaces for the LIVE of MnO electrode materials during electrochemical reaction.[25, 26] The relieving of the stress will increase its stability, which is effective in maintaining the MnO integrity for long-life LIBs. The carbon layer exhibited a high Li^+ conductivity. According to the equation of $\tau = L_{ion}^2 / D_{ion}$, where τ means the diffusion time, L means the ion diffusion length and D means the ion diffusion coefficient, the Li^+ diffusion coefficient in the carbon layer (Moved 880 nm in 191 s, Fig. 4c) is 4.0×10^{-11} cm^2 s^{-1}, which coincided well with the diffusion coefficient in other carbon materials reported previously.[27, 28] In addition, the Li^+ diffusion coefficient in the MnO-nanocore (Moved 37 nm in 616 s, Fig. S15a-e) is 2.2×10^{-14} cm^2 s^{-1}. The high diffusion coefficient of the carbon layer would contribute to the high-rate discharge ability. The experiments showed that the Li^+ intercalated in the MnO-nanocore came from the carbon layer, indicating a direct Li^+ transport through solid-solid interface. The interface transport would effectively reduce the Li^+ surface-to-core diffusion length and the diffusion time. It is a decisive process for improving the high-rate discharge ability. In short, the pre-LIVE behavior and the buffer effect of IVS made the carbon layer a rather stable structure to resist crack and fracture. The carbon layer presented a

high Li$^+$ diffusivity and acted as a path transporting Li$^+$ to MnO electrode materials through the solid-to-solid interface continuously at high speed and short route. Therefore, the improved cyclability of the MnO@C NRs constructed with a CSS and IVS was caused by the enhanced stability of carbon layer in the pre-lithiation and the buffer of the IVS. The improved high-rate capability was caused by the fast Li$^+$ diffusion of the carbon layer and the short pathway between the carbon layer and the MnO NR cores.
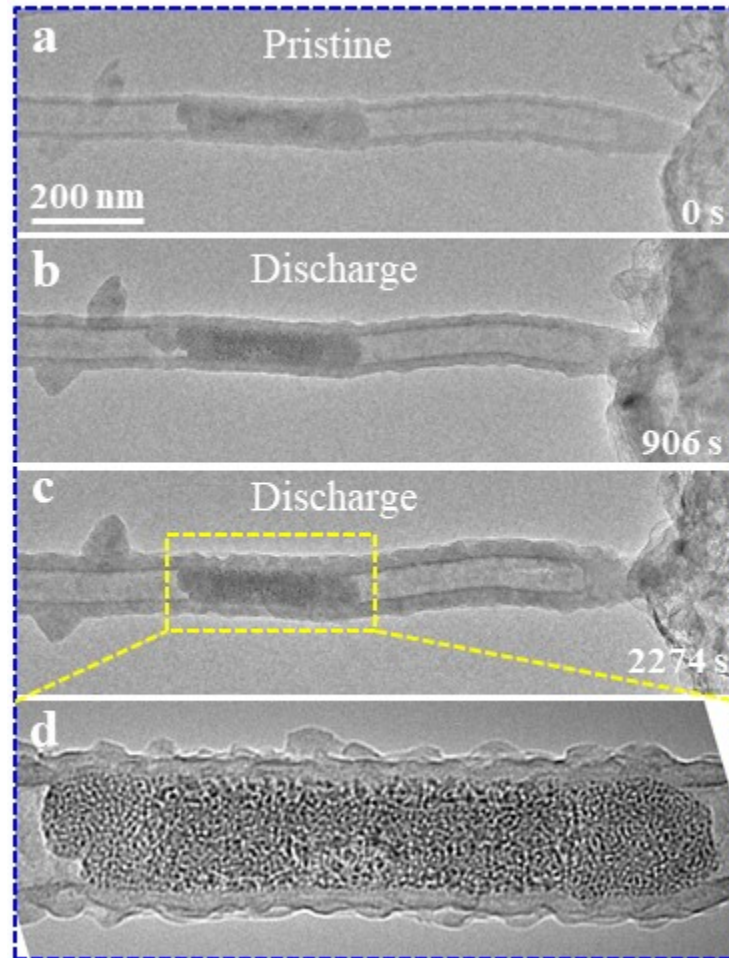

Fig. S16 Time lapse structure evolution of the MnO@C cathode in a Li-ion nanobattery during discharge processes.

In addition, we also did a deep discharge reaction for up to 2274 s using another MnO@C NR (Fig. S16). Similarly, the structure of the MnO NRs was destroyed, and a large number of Mn nanoparticles were formed. After both the discharge reaction of 1243 s (Fig. 3d) and the deep discharge of 2274 s (Fig. S16), it can be clearly found

that the MnO NR structure is destroyed.

Notes and References

1   Z. P. Ma, G. J. Shao, Y. Q. Fan, M. Y. Feng, D. J. Shen and H. J. Wang, *ACS Sustainable Chem. Eng.*, 2017, **5**, 4856.

2   Z. P. Ma, G. J. Shao, Y. Q. Fan, G. L. Wang, J. J. Song and D. J. Shen, *ACS Appl. Mater. Interfaces*, 2016, **8**, 9050.

3   Y. S. Tang, L. Q. Zhang, Y. F. Tang, X. Wang, T. Zhang, R. Yang, C. Ma, N. Li, Y. N. Liu, X. X. Zhao, X. H. Zhang, Z. F. Wang, B. Y. Guo, Y. F. Li and J. Y. Huang, *Chem. Comm*, 2019, **55**, 10880.

4   L. Q. Zhang, Y. S. Tang, Y. C. Wang, Y. L. Duan, D. G. Xie, C. Y. Wu, L. S. Cui, Y. F. Li, X. H. Ning and Z. W. Shan, *RSC Adv.*, 2016, **6**, 96035.

5   Q. N. Liu, T. T. Yang, C. C. Du, Y. F. Tang, Y. Sun, P. Jia, J. Z. Chen, H. J. Ye, T. D. Shen, Q. M. Peng, L. Q. Zhang and J. Y. Huang, *Nano Lett.*, 2018, **18**, 3723.

6   L. Q. Zhang, Y. C. Wang, D. G. Xie, Y. S. Tang, C. Y. Wu, L. S. Cui, Y. F. Li, X. H. Ning and Z. W. Shan, *RSC Adv.*, 2016, **6**, 11441.

7   G. Zhong, J. L. Yu, P. Y. Zhuang, M. Y. Jin, Y. B. Fu and X. H. Ma, *Electrochim. Acta*, 2019, **296**, 276.

8   Y. C. Xiao, C. Y. Xu, P. P. Wang, H. T. Fang, X. Y. Sun, F. X. Ma, Y. Pei and L. Zhen, *Nano Energy*, 2018, **50**, 675.

9   G. Y. Zhu, L. Wang, H. N. Lin, L. B. Ma, P. Y. Zhao, Y. Hu, T. Chen, R. P. Chen, Y. R. Wang, Z. X. Tie, J. Liu and Z. Jin, *Adv. Funct. Mater.*, 2018, **28**, 1800003.

10 W. Fu, T. Z. Liu, S. Hou, Y. Y. Guo, C. Mei and L. Z. Zhao, *J. Alloys Compd.*, 2021, **861**, 157961.

11 Z. L. Zhu, K. K. Bai, H. B. Zuo, E. Y. Ma, Z. Q. Xu and L. C. Liu, *J. Alloys Compd.*, 2019, **805**, 692.

12 J. G. Wang, H. Y. Liu, H. Z. Liu, Z. H. Fu and D. Nan, *Chem. Eng. J.*, 2017, **328,** 591.

13 K. Y. Li, F. F. Shua, X. W. Guo and D. F. Xue, *Electrochim. Acta*, 2016, **188**, 793.

14 C. B. Zhang, J. G. Wang, D. D. Jin, K. Y. Xie and B. Q. Wei, *Electrochim. Acta*,

2015, **180**, 990.

15   M. Gu, A. Kushima, Y. Y. Shao, J. G. Zhang, J. Liu, N. D. Browning, J. Li and C.M. Wang, *Nano Lett.,* 2013, **13**, 5203.

16   J. W. Wang, X. H. Liu, S. X. Mao and J. Y. Huang, *Nano Lett.,* 2012, **12**, 5897.

17   H. J. Ye, S. W. Gui, Z. F. Wang, J. Z. Chen, Q. N. Liu, X. D. Zhang, P. Jia, Y. S. Tang, T. T. Yang, C. C. Du, L. Geng, H. Li, Q. S. Dai, Y. F. Tang, L. Q. Zhang, H. Yang and J. Y. Huang, *ACS Appl. Mater. Interfaces,* 2021, **13**, 44479.

18   H. Zheng, Y. Liu, S.   X. Mao, J.   B. Wang and J.   Y. Huang, *Sci. Rep.,* 2012, **2**, 542.

19   S. H. Yan, K. P. Abhilash, L. Y. Tang, M. Yang, Y. F. Ma, Q. Y. Xia, Q. B. Guo and H. Xia, *Small*, 2019, **15**, 1804371.

20   J. Jin, L. Wu, S. Z. Huang, M. Yan, H. G. Wang, L. H. Chen, T. Hasan, Y. Li and B. L. Su, *Small Methods*, 2018, **2**, 1800171.

21   D. M. Xu, Y. F. Yang, L. F. Lyu, A. Ouyang, W. Liu, Z. Wang, L. L. Wu, F. Yang, J. R. Liu and F. L. Wang, *Chem. Eng. J.*, 2021, **410**, 128295.

22   Y. C. Xiao, C. Y. Xu, X. Y. Sun, Y. Pei, P. P. Wang, F. X. Ma and L. Zhen, *Chem. Eng. J.*, 2018, **336**, 427.

23   A. Chatterjee and S. W. Or, *Electrochim. Acta*, 2020, **338**, 135809.

24   S. J. Huang, H. P. Li, G. B. Xu, X. Liu, Q. Zhang, L. W. Yang, J. X. Cao and X. L. Wei, *Electrochim. Acta*, 2020, **342**, 136115.

25   Y. Zhao, L. P. Wang, M. T. Sougrati, Z. X. Feng, Y. Leconte, A. Fisher, M. Srinivasan and Z. C. Xu, *Adv. Energy Mater.*, 2017, **7**, 1601424.

26   M. Chen, Y. G. Zhang, L. D. Xing, Y. H. Liao, Y. C. Qiu, S. H. Yang and W. S. Li, *Adv. Mater.*, 2017, **29**, 1607015.

27   P. Yu, B. N. Popov, J. A. Ritter and R. E. White, *J. Electrochem. Soc.*, 1999, **146**, 8.

28   T. Uchida, Y. Morikawa, H. lkuta and M. Wakihara, *J. Electrochem. Soc.*, 1996, **143**, 2606.